Available online at www.sciencedirect.com
ScienceDirect
Journal of Sound and Vibration 313 (2008) 171–194
JOURNAL OF SOUND AND VIBRATION
www.elsevier.com/locate/jsvi

Shock wave impact on monolithic and composite material plates: The preferential aeroelastic response

Minwei Gong, Yiannis Andreopoulos*

Department of Mechanical Engineering, The City College of the City University of New York, Convent Avenue & 140th Street, New York, NY 10031, USA

Received 31 October 2006; received in revised form 9 November 2007; accepted 19 November 2007
Available online 10 January 2008

Abstract

An experimental investigation was carried out to determine the aeroelastic response of thin flat plates during face-on impact with planar shock waves. The experiments were performed in a large-scale shock tube research facility, which had a working section of 12″ in diameter and a length of 80 ft. One aluminum plate, one stainless steal plate and several composite plates were tested in the present investigation. Miniature semi-conductor strain-gauges of high-frequency response were employed to measure locally the strain on the exterior side of the plates and high-frequency response pressure transducers were used to measure time-dependent wall and total pressure. Due to the elastic deformation of the plates and their reverberation, strong acoustic waves were generated on the external side of the impact which carry a significant signature of the plates' properties. Composite plates were found to suppress several of the modes of the wave patterns while metallic ones demonstrate a rich variety of interacting modes. The amplitude of the excited acoustic waves, however, was higher in the case of composite plates than in the case of steel plates. The frequency content of the strain signals on the surface of composite plates was not always the same with the content of the surface acceleration measured in free vibration experiments. Calculations by using a coupled system of equations between the fluid and solid phases of monolithic materials provided predictions in good agreement with the measured values of modal frequencies. These theoretical results were also in agreement with the classical modal analysis results by using the Poisson–Kirchoff theory for thin plates under axisymmetric or non-axisymmetric conditions.

1. Introduction

The mutual interaction between a blast or shock wave and a structure is the subject of the present research program. Impingement of blast waves on structures can cause a reflection of the wave off the surface of the structure followed by a substantial transient aerodynamic load, which can cause significant deformation of the structure. This deformation can alter the overpressure, which is built behind the reflected shock. In addition, a complex aeroelastic interaction between the blast wave and the structure develops that can induce reverberation within an enclosure, which can cause substantial overpressure through multiple reflections of the wave. This problem is of particular importance in the new design of future army vehicles with composite

*Corresponding author. Tel.: +1 212 650 5206; fax: +1 212 650 8013.
E-mail address: andre@ccny.cuny.edu (Y. Andreopoulos).

0022-460X/$ - see front matter © 2007 Elsevier Ltd. All rights reserved.
doi:10.1016/j.jsv.2007.11.042

materials. It has been observed in the field that blast waves impinging on the external surface of army vehicles could induce substantial waves within the interior of personnel's compartment. Excessive levels of sound can cause permanent hearing loss and can be deleterious, both physiologically and psychologically, to one's health. The assessment of the effects of blasts on structural systems was studied systematically after World War I. The early published work was Hopkinson's study [1]. There exist some studies related to structures subjected to air-blast loading in the literature and one of the earliest analysis was performed by Taylor [2], where he developed a solution for one-dimensional (1D) wave impinging a free-standing plate to compute the momentum transmitted to the plate by the shock pulse. The prediction and measurement of the structural response of ship panels to free field air-blast explosions were first investigated by Houlston et al. [3]. In this research square plates and stiffened panels subjected to air-blast and underwater shock loads were investigated. Later, assuming a form of displacement function and a modified Friedlander reflected blast overpressure loading that exponentially decays with time, Gupta et al. [4] conducted a single-degree-of-freedom elastodynamic analysis of the response of a rectangular plate subjected to an explosive blast. Beshara [5] investigated the prediction of dynamic effects of unconfined explosions needed for the structural analysis of blast-loaded above-ground structures. Turkmen and Mecitoglu [6,7] carried out a study on the dynamic behavior of laminated composite plates subjected to blast loading. In his study, theoretical analysis and experimental results of the strain time histories were obtained. The behavior of steel plates in various configurations under air-blast loading was studied experimentally and computationally in Refs. [8,9]. However, all those aforementioned researches on the response of a structure to blast or shock wave impact are focussed on the structure alone. Very recently Zhenyu Xue and Hutchinson [10] studied the *quasi-static* dynamic responses of clamped circular sandwich plates subject to uniformly distributed impulsive loads. Numerical analysis on the plate neglecting the effects of fluid–structure interaction was carried out and a new constitutive relation for sandwich plates was introduced as well [11]. In a similar research [12,13], the dynamic response of a clamped sandwich beam/plate was assessed. The fluid–structure interaction effect was evaluated utilizing Taylor's [2] approximation by including a segregated *fluid– structure interaction phase* in their research. However, the interaction between the blast and the structure is mutual. The structure is deformed by the blast loading and its deformation affects the blast reflection itself on the inner side of the structure where the blast impacts and excites acoustic disturbances which may be quite strong to be developed in a weak shock wave on the outer side. The aeroelastic coupling between the structure and the blast loading is not fully understood. In particular, the complicated resonance caused by the blast loading on the structure and the flow phenomena associated with sound excitation and shock waves reflections mentioned above have not been fully investigated. The present work focuses on better understanding the aeroelastic response of metallic/monolithic and composite materials to blast or shock wave impact. These complicated interactions are investigated by using a simple, yet relevant geometry and simplified flow fields which have the potential to reveal basic features of the associated phenomena. Along these lines the following experiments were carried out:

1. Plane shock wave impacting "face on" a thin aluminum flat plate.
2. Plane shock wave impacting "face on" a stainless steel flat plate.
3. Plane shock wave impacting "face on" composite material flat plates (see Fig. 1).

The pressure wave generated by a blast propagates in the form of a shock wave with a spherical wavefront away from the source. A blast wave is typically comprised of a compressional wave, which is followed by a rarefaction or an expansion wave. High shearing rates however occur during the impact of the shock wave front on the structural element because of the extremely short time scales of the shock impact duration. Relaxation of this high shearing rate takes place immediately after the shock wave impact during the passage of the expansion wave which is associated with time scales that are 10^3 times or more lower than those of the shock wave.

Depending on the time scales of the blast wave and that of the structure, the structure response to a blast loading can be categorized as the following [14]:

Impulsive response: The load pulse is short compared to the natural period of vibration of the structure so its response can be determined by applying the load pulse in the form of kinetic energy to the structure, which subsequently deforms and acquires strain energy.

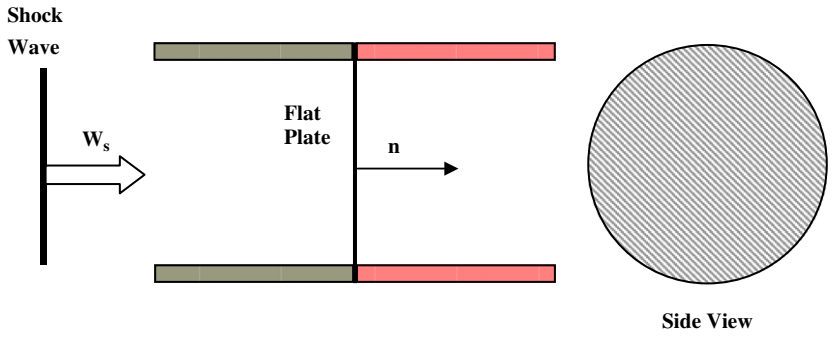

Fig. 1. Plane shock wave interaction with thin flat plate.

Quasi-static: Pressure load duration is long compared with the natural response time of the structure. The blast will cause the structure to deform whilst the loading is still being applied. The loading does work on the structure, causing it to deform and acquire strain energy.

Dynamic or pressure time: Load duration and structural response time are similar; the equation of motion of the structural system is needed to solve the structural response.

In order to simplify the complexity of the problem, the present investigation focuses only on the shock wave part of the blast wave. In addition, due to the short time scales associated with the shock wave impact, shearing/strain rates are higher than the rates developing during the expansion wave phase and therefore their role in the dynamic behavior of the structure may be more significant than the slow relaxation of the loading during the passage of expansion waves. Thus in the present context, a shock wave generated in a shock tube facility impacting on plate specimens will be considered in all interactions.

The present approach to use a shock tube platform appears to have certain distinct advantages over approaches using of detonations. The major one is that the shock front in the shock tube is planar, thus yielding uniform pressure behind it which loads the structure. This simplifies the geometry and boundary conditions and therefore it allows for a better evaluation of modelling issues associated with numerical simulations of the phenomena involved. In contrary, shock wave fronts generated by detonations are three dimensional in space and lead to complex pressure loadings which can mask the underlying basic physics of the impact. Once the physics of the impact is better understood in simple geometries then the next level of complication can be introduced.

2. Physics of the interaction

A shock wave is considered travelling in a shock tube with a flat plate mounted at the end wall. The pressure behind the incident shock wave, p_2, remains constant across the flow field before the shock reflection. As the shock wave touches the surface of the end wall the process of reflection starts, the plate is loaded and deformation begins. If the plate were a rigid body the pressure behind the reflected shock, p_5, would be given by the relation

$$\frac{p_5}{p_2} = \frac{[(\gamma+1)/(\gamma-1)+2](p_2/p_1)-1}{p_2/p_1+[(\gamma+1)/(\gamma-1)]}. \tag{1}$$

In this relation, p_1 is the pressure ahead of the moving shock wave, p_2 is the pressure behind the shock wave and p_5 is the pressure behind the reflected shock wave which causes the aerodynamic load on the structures and γ is the ratio of specific heats c_p/c_v (see Ref. [15]). This pressure ratio is always greater than 1 indicating that consecutive reflections tend to increase the pressure behind each reflection substantially. The reason is that the kinetic energy of the moving shock wave and the flow behind is converted to potential energy after the reflection because the flow has to acquire the velocity of the reflecting boundary which is zero. Even for weak shock waves with typical $p_2/p_1 = 1.5$, the pressure behind a flat wall reflection is $p_5/p_1 = 1.5 \times 1.47 = 2.2$. However, when the plate is elastic, its deformation starts the moment load is applied during the initial contact

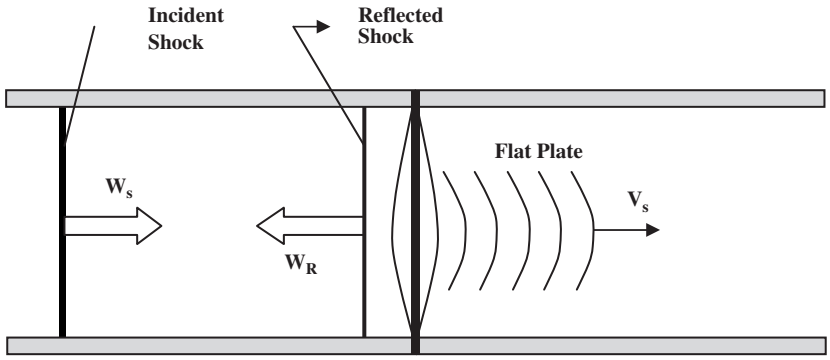

Fig. 2. Sound waves excitation through shock impingement.

between the shock wave and the surface. If we assume that the plate structure is rigid and that the shock wave is a discontinuity then its reflection takes place instantaneously and the pressure p_5 is applied also instantaneously on the plate. In that respect this is the loading pressure of the plate since the flow velocity behind the reflected shock is zero. In the case of an elastic plate Eq. (1) is not valid and the aerodynamic load will reverberate the plate. During the initial displacement of the accelerating plate towards the $x>0$ direction, expansion waves will be shed off in the direction of the reflected shock ($x<0$) and compression waves in the opposite direction on the external side of the plate. During the decelerating displacement of the plate in the other direction compression waves will be shed in the $x<0$ direction behind the reflected shock wave and expansion waves in the exterior side of the plate (see Fig. 2).

The presence of compression or expansion waves will result in changes in the fluid pressure in either side of the plate. More details of the interaction between the shock wave and the elastic surface can be explored if the shock wave is assumed of finite thickness with continuous distribution of pressure or velocity across. The mutual interaction between the impacting shock wave and the solid plate has been modelled by using one theoretical and two numerical simulations.

In addition to the experimental work the theory of Poisson–Kirchoff was employed first to solve analytically [16] the partial differential equation of motion for the axisymmetrically loaded plate. In the second method, numerical simulations of the same equation were obtained. In these two methods the fluid flow and plate equations were decoupled. Numerical simulations of the coupled system of the solid with the fluid phase equations were carried out in the third method. In this case the basic equations solved in a finite element formulation were used.

3. Experimental techniques

The experiments were carried out in the large-scale shock tube research facility of the Department of Mechanical Engineering at CCNY which is schematically shown in Fig. 3. The facility is described in detail by Briassulis et al. [17] and has been used extensively for research on shock wave interactions with turbulence and vortices [18–20]. The rupture of the diaphragm in the driver's section generates a shock wave which travels downstream towards the end wall where the plates are mounted. The plates used in this investigation were inserted in the last flange before the dump tank. The plates were clamped between the female and male parts of the flange by using a protective rubber gasket. Pressure was applied uniformly on the plates through 8 bolts of the flange.

High-frequency response, semi-conductor, micro-strain gages made by Kulite Semiconductors were properly attached on several locations on the external surface of each plate in order to measure the transient strain rate during the "face-on" impact of the shock wave. Fig. 4 shows the experimental arrangement. Two wall pressure transducers and one total pressure transducer were used to monitor the flow and trigger the data acquisition. Two pressure transducers were placed on the other side of the thin plate at the end of the shock tube. One transducer was mounted on the wall to measure static pressure and another at the tip of a holder to

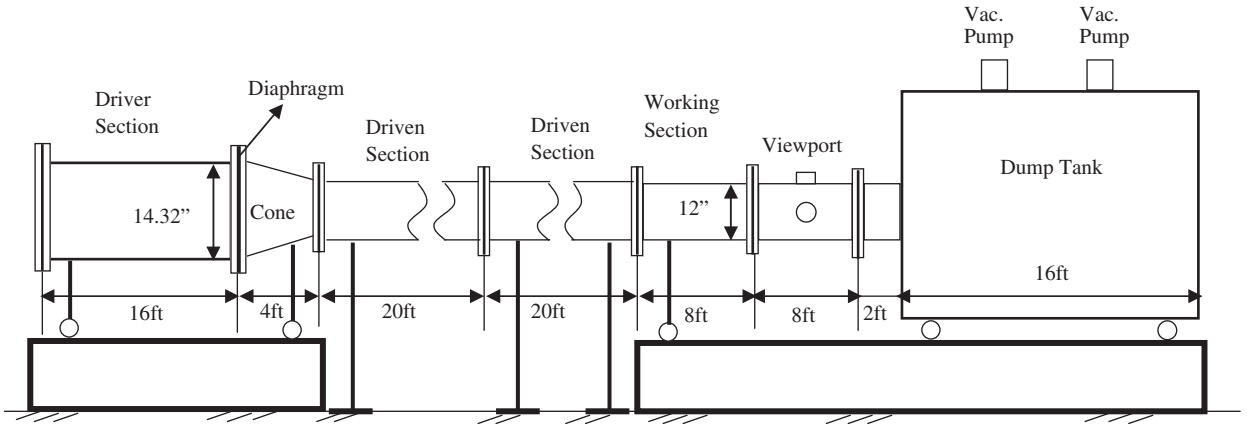

Fig. 3. Schematic of shock tube research facility.

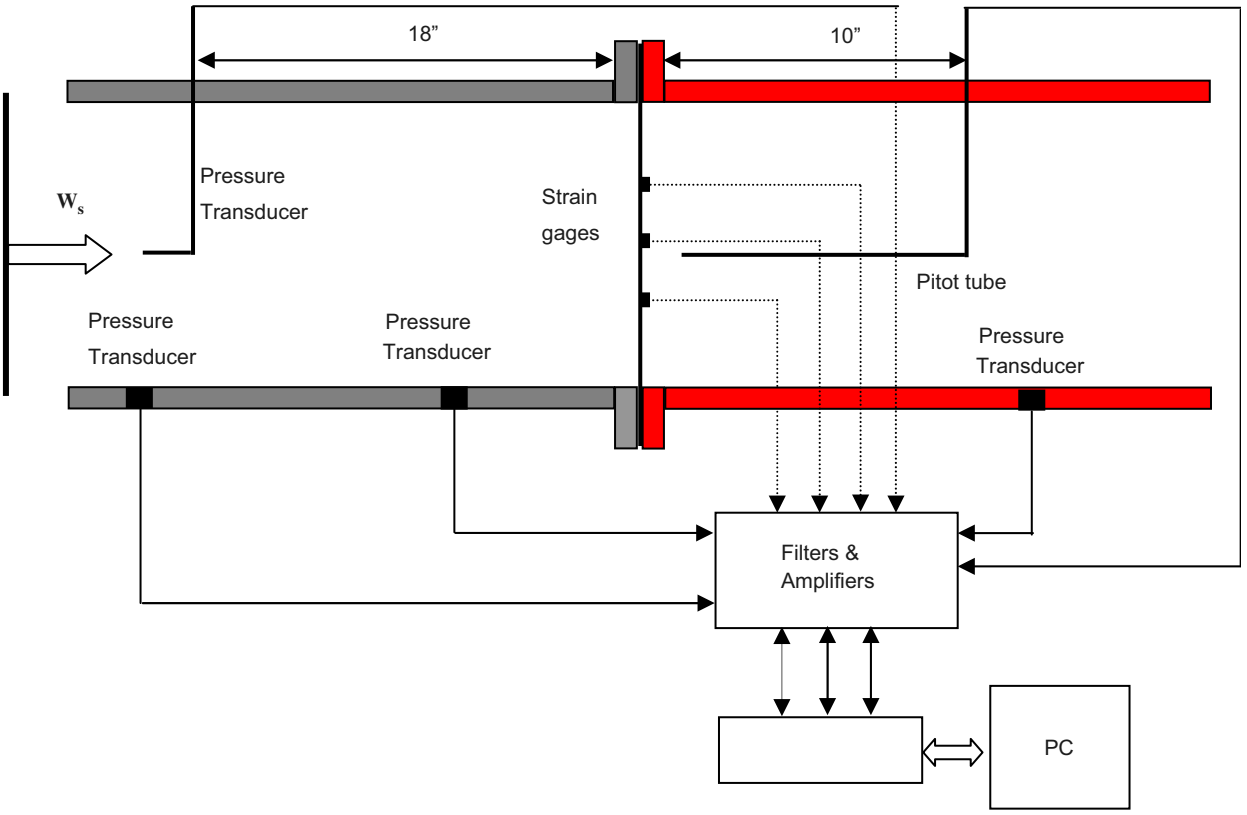

Fig. 4. Experimental setup.

measure total pressure inside the flow. All transducers were sub-miniature in size, model XCQ-062, with sensing area of 1 mm in diameter, made by Kulite Semiconductors. The wall mounted transducers and the one used as pitot tube probe in the upstream of the plate flow region had a range up to 150 psi. The transducer used as a pitot tube in the downstream of the plate region had a range of 0–5 psi. Their frequency response was limited by their resonance frequency at 150 kHz.

Dimensions of the plates and their material properties are given in Table 1. Each plate had an outer diameter of 14.5″ and they were mounted on the end flange of the shock tube which had an internal diameter

Table 1
Plate dimensions and material properties

(a) Plate	Plate Material	Thickness	Diameter	Young's modulus, E (GPa)	Poisson's ratio	Density (kg/m^3) $\times 10^3$
#1	Aluminum plate	0.125″	14.5/12″	71	0.33	2.7
#2	Stainless steel plate	0.0625″	14.5/12″	205	0.3	7.7
#3	Composite plate (isotropic)	0.220	14.5/12″	33	0.25	1.81

(b) Plate	Plate material	Thickness	Diameter	Young's modulus, E (0^o direction) (GPa)	Density (kg/m^3) $\times 10^3$
#4	Composite plate $[0]_{12}$	0.125″	14.5/12″	65.1	1.72
#5	Composite plate $[0, 90]_6$	0.125″	14.5/12″	38.9	1.72
#6	Composite plate $[0, 45, -45, 90]_3$	0.125″	14.5/12	29.6	1.72

of 12″. The composite plate is laminated with 10 individual woven fabric layers each with orientation $[0, 90]_6$ which resulted in a quasi-isotropic plate with practically no preferential direction of its fibers. The Young's modulus of the composite plate is obtained through a tensile test performed on a MTS-810 test system in the *Material Processing & Solid Mechanics Lab* at *CCNY*. The locations of the strain gages on each plate are shown in Figs. 5a–d.

Type-UHP5000-60 micro-strain gauges fabricated by Kulite were used in this work. They have a size of 0.5 mm × 0.75 mm. They possess a frequency response of 10 kHz, high sensitivity (gage factor of 175) and high signal-to-noise ratio (15:1). Their miniature size allows for localized measurement of strain. Fig. 5e shows a schematic of the strain gage, and Fig. 5f shows a picture of a composite plate with two strain gages mounted. Mounting and wiring these sub-miniature strain gauges on each of the plates required special attention and skills. They were first positioned on the plates with the help of a microscope and glued by using epoxy. Immediately after they were mounted, they were placed in an oven for several hours so that the epoxy was cured and a strong bond between the gage and the plate was created that allowed for a "point" measurement of the local strain without slippage between the surface and the gage. The plate was then mounted on the shock tube.

The strain gages were mounted on the non-shock impact exterior side, such that the thermal effects on the strain gages caused by the temperature fluctuations within the flow can be minimized. With such configuration, during the shock impact, the strain gages near the edge of the plate will be expected to undergo compression and result in a negative strain value. Strain gages mounted near the center of the plate are expected to have a positive value while experience tension. Such variation of exterior surface strain in the radial direction was illustrated in Fig. 5g. The transition from positive to negative strain occurs at $r = 0.628R$ and the maximum absolute strain is at the boundary of the plate.

The strain gauges were calibrated "in situ" by applying a known static pressure in the enclosed shock tube and recording the output voltage. A linear relation between output voltage and measured strain was found as expected.

The present work required the implementation of a new high-speed data acquisition with high resolution for simultaneous recording of all time-dependent signals. Four analog-to-digital boards type DATEL-416G A/D with two input channels each were synchronized to simultaneously acquire data. These boards are mounted on PCI slots of PCs and acquire data with a rate of 1.0 MHz and 14 bits resolution. At this time, they represent the state-of the-art in "off the self" A/D boards. New software has been developed to interface the boards and drive the data acquisition and data transfer. A new trigger circuit was also designed and implemented. In addition custom-made digital signal processing software was developed in C/C++/Assembly language. A total of 100 ms of data duration was recorded.

The natural frequencies of the aluminum, stainless steel and quasi-isotropic composite (#3) plates were determined by impacting them in situ by a sphere mounted on a string. This point impact represents a delta

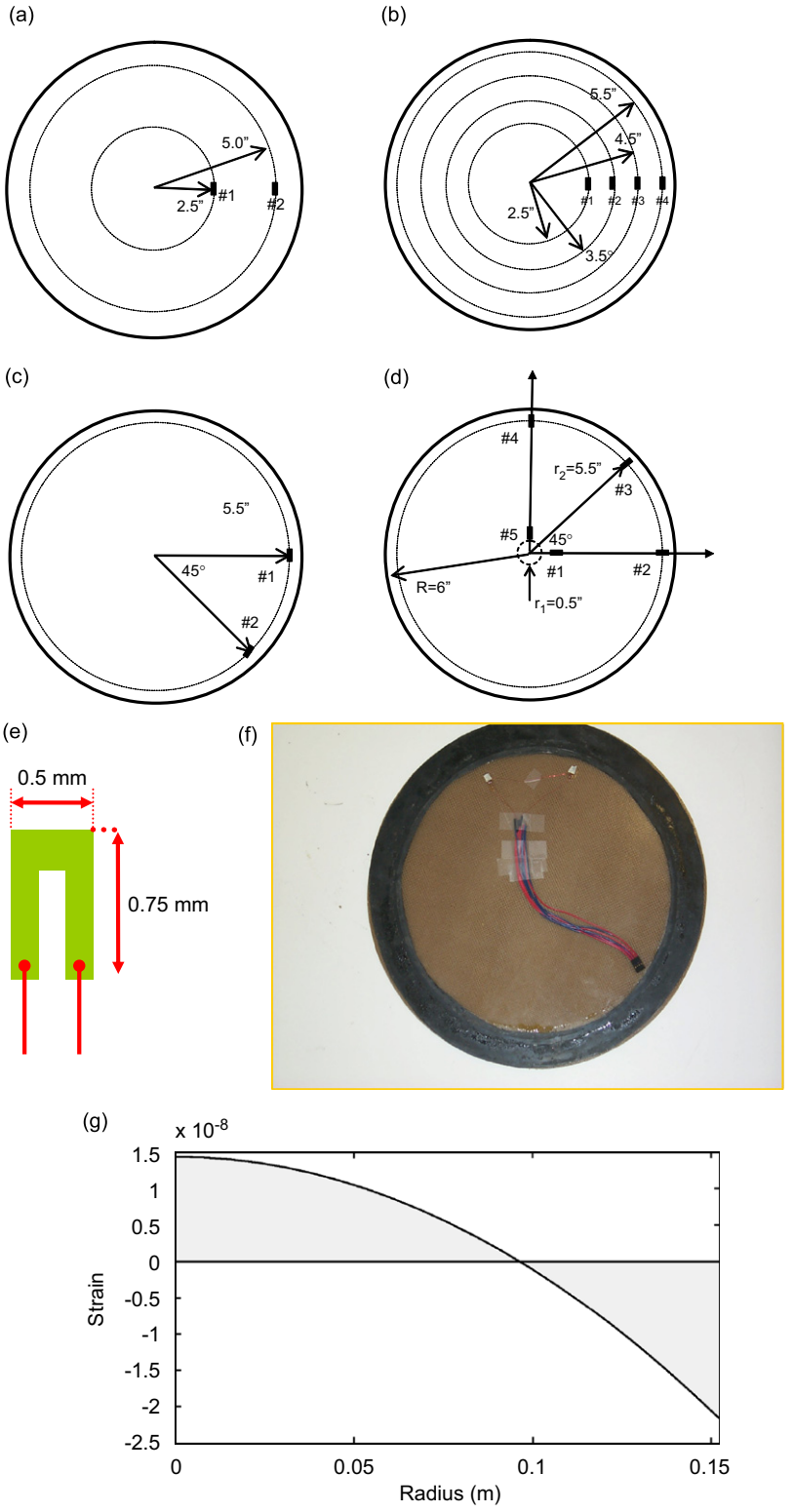

Fig. 5. (a) Strain gage locations on aluminum plate; (b) strain gage locations on stainless steel plate; (c) strain gage locations on quasi-isotropic composite plate; (d) strain gage locations on composite plates; (e) semi-conductor micro-strain gage; (f) picture of composite material plate with mounted strain gages; and (g) strain variation in radial direction at the external surface of a fully clamped aluminum plate under uniform unit load applied at its internal surface.

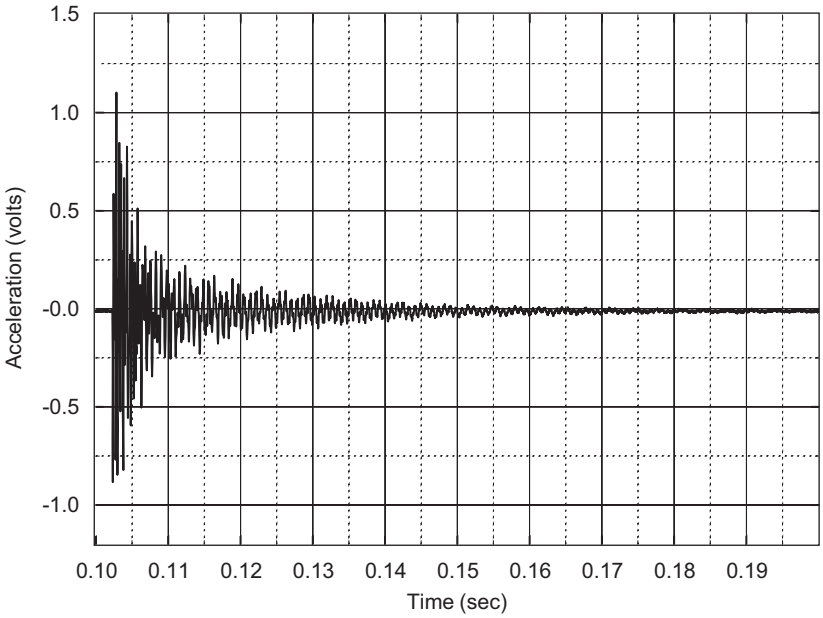

Fig. 6. Typical accelerometer signal during free vibration experiments with composite plate #3.

function with a uniform Fourier transform. The output of an accelerometer was used to provide the time-dependent signal for frequency analysis. The experiments were repeated several times with the accelerometer placed at different locations on the plates. A typical accelerometer output signal is shown in Fig. 6. It has been obtained in the free vibration experiments with the composite plates #3. It clearly demonstrates a strong decaying behavior characterized by a damping in the amplitude of the oscillations.

The modes obtained from these free vibration data are tabulated in Table 2a–c. An attempt has been made to identify and sort out the peaks in the spectrum according to the Poisson–Kirchoff theory highlighted in Section 5.1.

The effects of damping which are responsible for the decaying characteristics of the acceleration or strain signals have been also considered to determine their effect on possible modes shifting on the spectrum. The impulse response function of a single-degree-of-freedom system with viscous damping, as the present one, can be obtained by linear superposition of the effects of individual modes, assuming decoupling is possible [21]:

$$h_n(t) = A_n\, \mathrm{e}^{-\xi_n\omega_n(t-t_0)}\, \cos((1-\xi^2)^{1/2}\omega_n t),$$

where ω_n is the modal frequency, $\xi_n\omega_n$ is the damping constant, $\omega_{d,n} = (1-\xi^2)^{1/2}\omega_n$ is the pseudo-pulsation, φ_n is the phase of the nth mode and A_n is the amplitude of the nth coordinate of the mth mode.

The Fourier transform of $\mathrm{e}^{(-\xi_n\omega_n(t-t_0))}$ is $(\xi\omega_n - \mathrm{i}\omega)^{-1} + (\xi\omega_n + \mathrm{i}\omega)^{-1}$ and its convolution with a series of cosines which represents the signal, has modes shifted from $(\pm\mathrm{i}\omega_n)$ to $(\pm\mathrm{i}\omega_{d,n})$, i.e. its Fourier transfer of $h(t)$ is $2\xi\omega_n/[\xi^2{\omega_n}^2 + (\omega - \omega_{d,n})^2]$. If a value of $\xi = 0.30$ is assumed then the modal shift is only 4.5%. Thus the main effect of the decay is to broaden the modal peaks particularly at low frequencies.

4. Results

4.1. Shock wave impact on isotropic plates

Most of the results presented here obtained in experiments with a pressure ratio $p_2/p_1 = 1.49$ across the incident shock wave. In this set of experiments, all the signals of pressure transducers and strain gages shown in Fig. 4 were recorded. Additional experiments at different pressure ratios and different mounting locations of strain gages were also recorded without the pressure information downstream of plate (see Ref. [22]).

Table 2
Modal analysis results and comparison with experimental data for (a) aluminum plate, (b) stainless-steel plate and (c) quasi-isotropic composite plate

	Mode n	Mode m				
		1 (Hz)	2 (Hz)	3 (Hz)	4 (Hz)	5 (Hz)
(a) *Aluminum plate*						
Theoretical calculation without coupling	1	348	1356	3040	5396	8427
	2	725	2075	4096	6791	10159
	3	1190	2886	5248	8281	10159
Numerical simulation without coupling		348.5	1356.9	3040.2	5398.0	8431.6
Numerical simulation with coupling	1	333.4	1334.9	3015.2	5371.3	8404.0
Experimental data: Shock impact	1	335	1373	3080	5436	
	2	732	2075	4058		
	3	1190	2838	5157		
Experimental data: Free vibration	1	–	1340	–	5938	
	2	–	2100	3739	7258	
	3	–	2859	4800	8578	
(b) *Stainless steel plate*						
Theoretical calculation without coupling	1	173	675	1513	2686	4195
	2	361	1033	2039	3381	5057
	3	592	1436	2612	4122	5057
Numerical simulation without coupling		173.5	675.5	1514	2687	4198
Numerical simulation with coupling	1	168.2	667.7	1504	2676	4185
Experimental data: Shock impact	1	184	701	1499	2655	4150
	2	335	1068	2197	3326	5001
	3	549	1373	2410	4150	5257
Experimental data: Free vibration	1	–	760	–	2859	
	2	–	980	1780	3499	4979
	3	520	1360	2300	4239	
(c) *Composite plate #3*						
Theoretical calculation without coupling	1	498	1938	4343	7711	12,040
	2	1036	2965	5853	9703	
	3	1700	4123	7498	9703	11,832
Numerical simulation without coupling		497.8	1938	4342	7710	12,043
Numerical simulation with coupling	1	479.5	1911	4310	7673	12,002
Experimental data: Shock impact	1	396	1953	4700	7200	–
	2	1220	2600	5859	–	–
	3	1700	4500	–	–	–
Experimental data: Free vibration	1	320	1919	4740	7380	–
	2	1240	2760	5798	9938	–
	3	–	4300	7258	–	–

Fig. 7 shows a typical pressure signal obtained by a wall pressure transducer located in a position upstream of the plate, in the experiment with the aluminum plate. The two jumps in the pressure signal are caused by the passage of the incident and reflected shock waves above the transducer. There is a mild overpressure spike by the incident shock wave pressure jump which is associated with partial reflection of the shock over the sensing area of the transducer [23]. The pressure behind the incident shock remains constant with some minor fluctuations.

The flow behind the reflected shock acquires the velocity of the reflecting wall which in the case of rigid wall is zero and therefore the energy of the incident flow is converted into potential energy. The theory predicts a pressure $p_5 = 17.9$ psig behind the reflected shock, a value which is slightly lower than the measured pressure of 18.2 psig shown in Fig. 7. The sudden deceleration of the fluid flow is accompanied with large pressure fluctuations behind the reflected shock which are associated with the increase of scale and magnitude of turbulence that is amplified by the interaction of the reflected shock with the boundary layer developing over the shock tube wall [24].

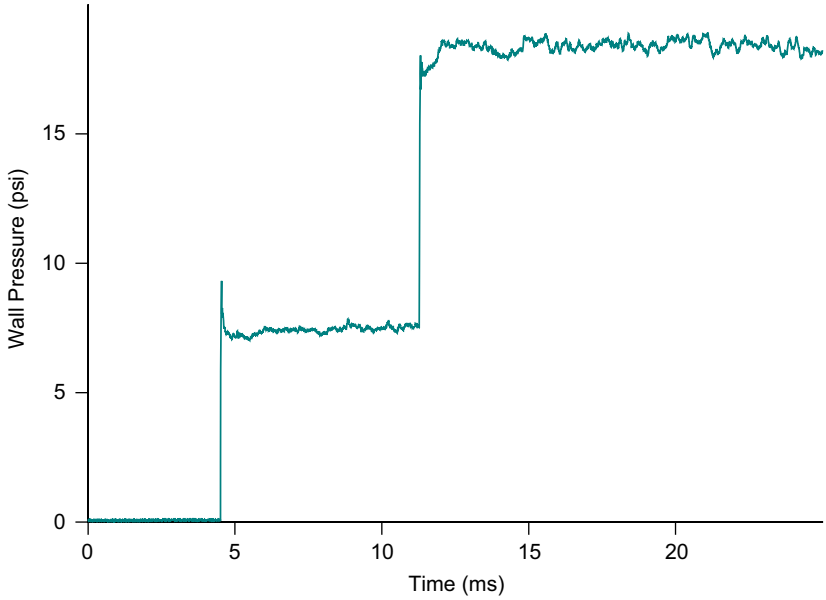

Fig. 7. Typical wall pressure signal: first rise, incident shock and second rise, reflected shock.

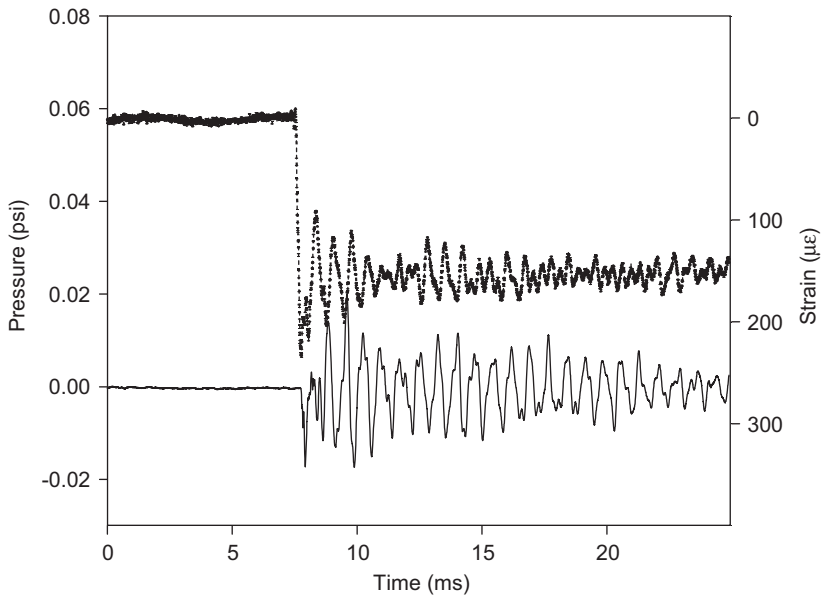

Fig. 8. Signal of strain gauge and resonance pressure signal in the case of aluminum plate. Black solid line, resonance pressure and dotted line, strain.

Fig. 8 shows one typical strain gauge signal obtained in the experiment with the aluminum plate. In the case of strain gage signals, the incident shock is reflected at the same longitudinal position where the strain gages are located and at the same time in all of them. As a result of the combined incident and reflected shocks one signal jump only can be observed in the strain signal. The strain signal obtained with gage #2 remains always negative due to compression at the outside surface of plate near the position of clamping where the strain gauge is mounted at $r = 5''$.

The resonance pressure signal obtained by the pitot tube on the exterior side, across the plate, is also shown in Fig. 8. Peak-to-peak fluctuations of the order of 0.02 psi in amplitude can be observed. The signal shows an

initial jump, which is about 0.2 ms after the onset of the initial shock impact on the strain signal. The pressure signal exhibits a considerable amount of periodicity which is correlated well with the periodicity of the corresponding strain signal with which there is a phase difference. It is interesting to observe that the pressure signal although initially followed the strain signal, it is ahead of it before the end of the first period.

A frequency analysis of the signal by using fast Fourier transforms indicated the existence of several peaks in the spectrum (see Fig. 9a). Several other frequencies multiple of the above were also found. It appears that a complicated wave pattern exists within the reverberating plate, which starts as soon as the shock gets in contact with the plate and gets reflected off the plate. This wave pattern may consist of compressive P-wave, shear SH—and/or SV-waves. The waves with time scales of microsecond reflect from the circular boundary which holds the plate and interact with themselves in a manner not yet understood to produce the vibration patterns of the plate which appear with time scales of the order of millisecond. The free vibration modal data obtained from the accelerometer during the sphere impact experiments are shown in Fig. 9b and they appear to be in reasonable agreement with those derived from the forced vibration measurements. No subharmonic or first modes were detected in the free vibration data which could be attributed to nonlinear effects associated with plastic deformation of the aluminum plate since the same plate was used in the free vibration experiments which were carried out after the shock impact experiment.

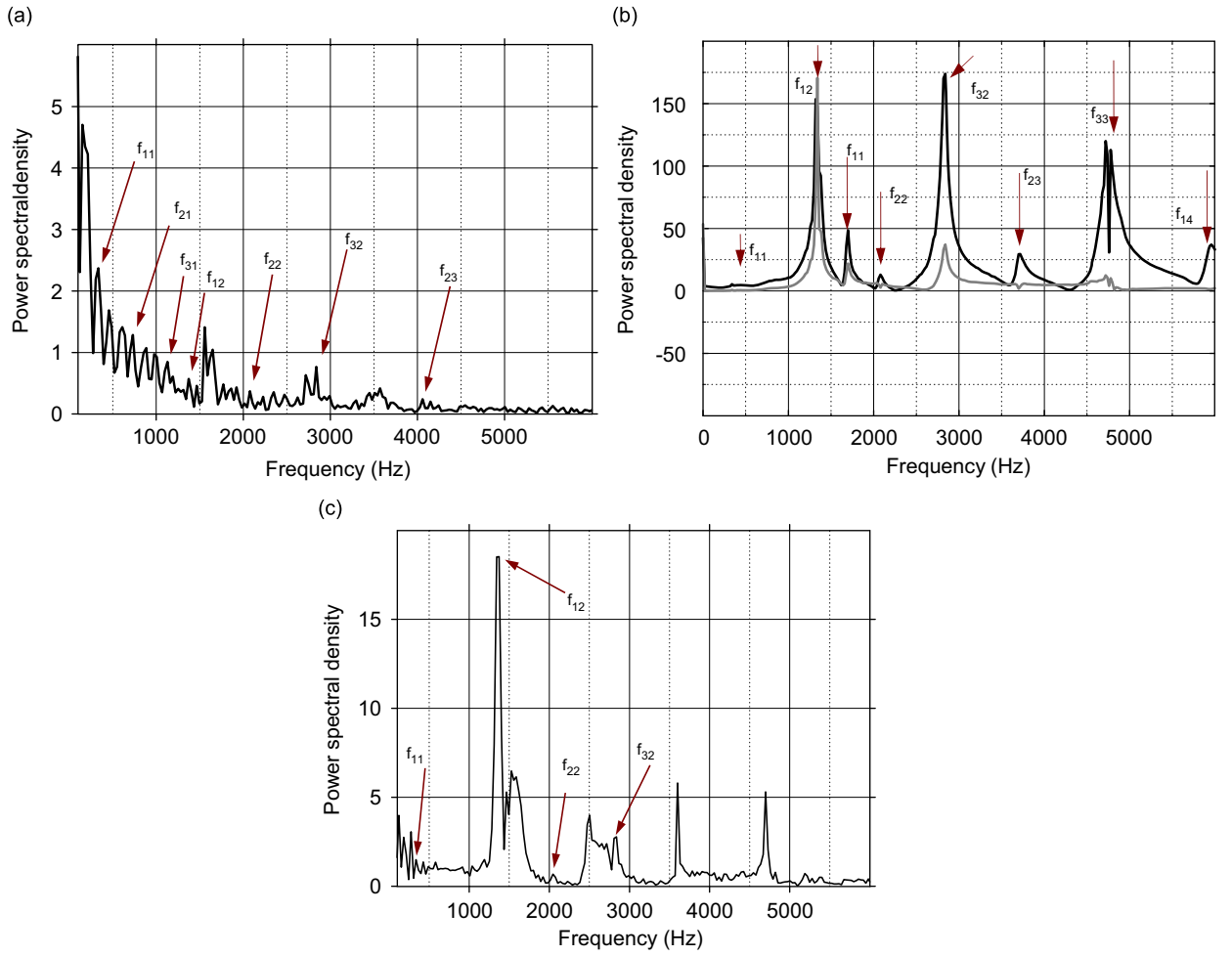

Fig. 9. (a) Power spectral density of strain gauge signal on aluminum plate during shock wave impact. Arrows point modes according to Poisson–Kirchoff theory. (b) Power spectral density of accelerometer signal on aluminum plate in free vibration experiments. Arrows point modes according to Poisson–Kirchoff theory. (c) Power spectrum density of pressure excited by the reverberating aluminum plate. Arrows point modes according to Poisson–Kirchoff theory.

Several of the peak frequencies shown in the spectrum of strain are also present in the spectrum of resonance pressure shown in Fig. 9c. The results of the modal analysis of the plate under shock impact are tabulated in Table 2a and are sorted out according to the Kirchoff–Poisson theory described in next section. They indicated that several modes of forced vibrations are at frequencies 335, 1373 and 2838 Hz, respectively. The data show the presence of a subharmonic mode at 164 Hz which has been also found in Ref. [25]. This scales with the speed of sound and the shock tune diameter $c/2\pi D = 170$ Hz, which suggests a possible Helmholtz resonance. The strong damping characteristic of the signals causes substantial broadening in the power spectrum at low frequencies which results in some ambiguity in differentiating the modes.

The signals of strain and resonance pressure in the case of the stainless steel plate are shown in Fig. 10. Periodicity is also evident in the signals. The strain is positive in both signals since the strain gages were mounted closer to the center of the plate. Spectra of the signals are shown in Figs. 11a and c. The modes (1,1), (2,1), (3,1), (1,3) and (3,3) are the dominant ones in the strain signal. The resonance pressure spectrum of the excited flow field at the other end of the plate show peaks at about the same frequencies as the strain spectrum. The modes detected in the acceleration spectrum during the free vibration experiments are shown in Fig. 11b. They agree within 5–20% from those in the shock loaded forced vibration experiments. The symmetric modes (1,1) and (2,1) have not been excited in free vibration.

In the case of plates made of composite materials, the signals, shown in Fig. 12, are considerably "cleaner" than in the cases of steel or aluminum plates. In fact, the spectra shown in Fig. 13a indicate one major peak at 396 Hz only. Several other modes with considerably smaller amplitudes are also present. The free vibration spectra of acceleration, presented in Fig. 13b, show several modes at higher frequencies. This is a remarkable difference in the modal content of acceleration and strain.

The spectrum of the resonance pressure in Fig. 13c, obtained in shocked vibrations shows several major peaks, indication of presence of several modes in the signal. This is also evident in the signals shown in Fig. 12 where the strain signal show a periodicity with frequency of 396 Hz, while the resonance pressure signal contains this frequency as well as higher ones. Two strain gauges, located in at the same radial distance from the center were used in this experiment with the composite plate #3. One gage, however, was rotated 45° to the direction of the local radius. The fact that the signals of the two strain gauges are identical indicates that this 10-layer composite has an isotropic behavior. It is obvious from the above experiments that the impact of the shock sets the plate in motion, which then excites waves in the other side. The amplitude of the waves is quite large, 0.025 psi (140 dB) indicating that the wave itself may be stronger than a simple sound wave.

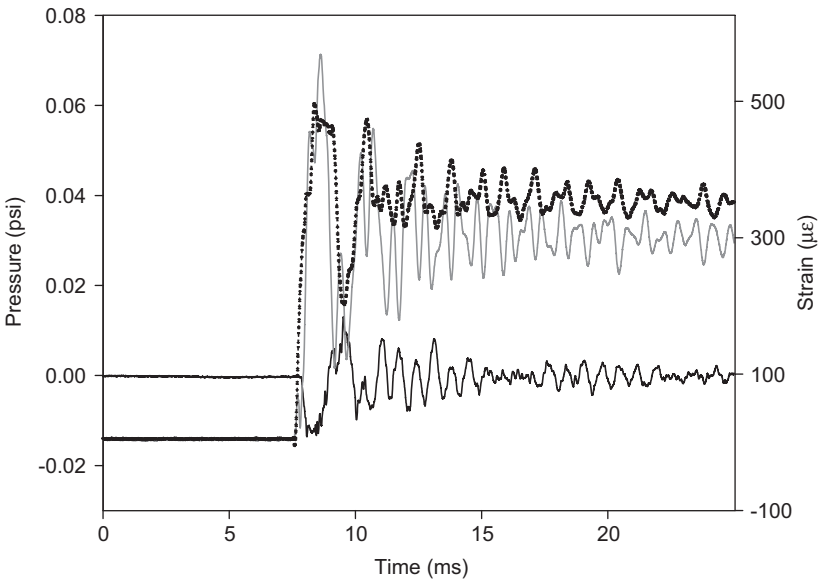

Fig. 10. Signals of strain gauge and resonance pressure in the case of stainless-steel plate. Solid black line, resonance pressure; dotted black line, strain; and gray line, strain.

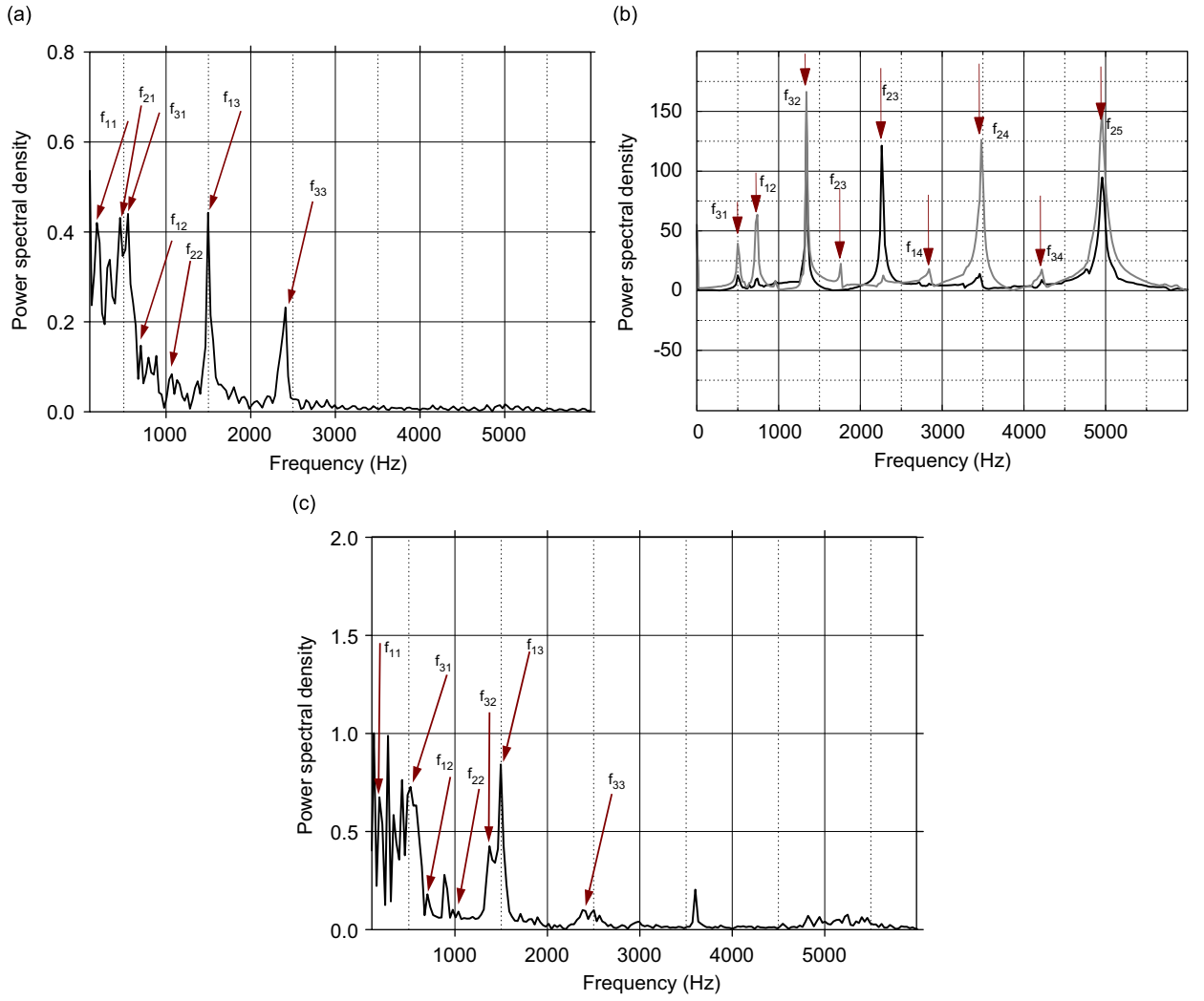

Fig. 11. (a) Power spectral density of strain gauge signal on stainless-steel plate during shock wave impact. Arrows point modes according to Poisson–Kirchoff theory. (b) Power spectral density of accelerometer signal on stainless-steel plate in free vibration experiments. Arrows point modes according to Poisson–Kirchoff theory. (c) Power spectral density of the pressure excited by the reverberating stainless-steel plate. Arrows point modes according to Poisson–Kirchoff theory.

The frequency spectrum of the pressure signal has one peak at 396 Hz which corresponds to a peak in the spectrum of the strain at the same frequency. Several other peaks observed in the pressure spectrum appear to be substantially dampened in the strain spectrum. This is a very intriguing behavior of composites which needs to be investigated further.

The power spectrum of the acceleration signal, shown in Fig. 13b, exhibits several modes of substantial strength throughout the whole frequency range. The first mode at 320 Hz is reasonably close to the 396 Hz observed in the shock loaded experiments which also indicated a peak at 182 Hz, most probably a subharmonic component.

The present experimental results show that plates made of different materials exhibit a distinct modal response when subject to shock wave loading. It is quite clear that the motion of the composite plates, as it is depicted by the accelerometer, is not physically different from the motion of monolithic plates. The strain field in the shock loaded case, however, exhibits different behavior. The experiments with quasi-isotropic composite plates indicated that the shock impact results in one dominant mode of stress waves only which indicate that it may be caused by mechanisms that are not present in the cases of metallic plates. Although the strain field

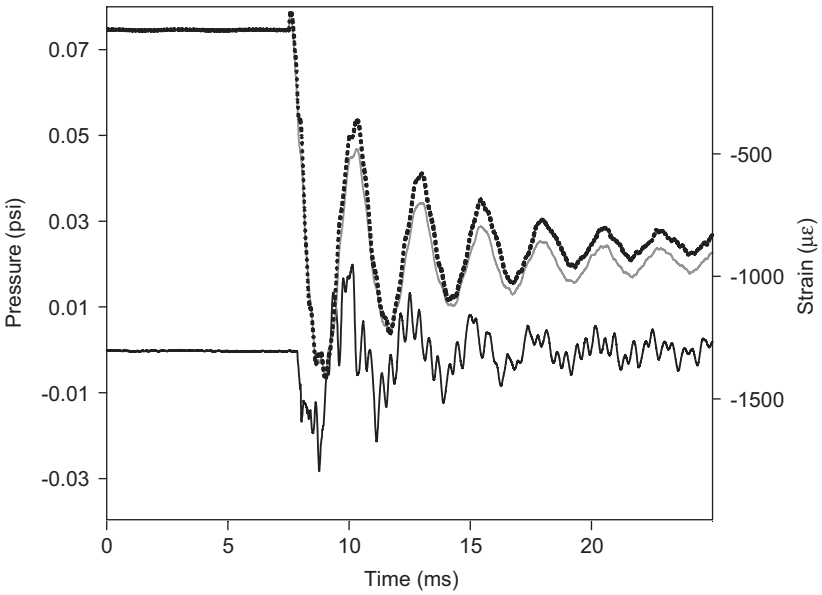

Fig. 12. Signal of strain gauge and resonance pressure signal in the case of composite plate. Solid black line, resonance pressure; dotted black line, strain; and gray line, strain.

indicates considerable damping of several of the modes, all modes were observed in the acoustic resonance signal. It was also observed that there exist several additional peaks in the resonance signal power spectrum; they may belong to the subharmonic and high harmonics of the acoustic excitation. Such acoustic excitation is nonlinear and further investigation is needed in order to better understand this behavior. Damping of the plate vibration in time was also observed on all plates during the interaction but the mechanism is still not yet known. It is still not determined whether such damping is mainly caused by the acoustic excitation or the material's viscoelastic behavior.

4.2. Shock wave impact on non-isotropic plates

Several experiments using composite plates with various properties were also carried out. The experimental arrangement is the same as described above. The composite plates and their properties are listed in Table 1b. The strain gage locations are shown in Figs. 5d and f. The power spectra of the strain and reverberating signals are shown in Figs. 14a, b, and 15a, b. Periodicity is evident in these signals and all strain signals posses a peak at around 900 Hz. However, because the composite plates used in these experiments are no longer isotropic, the magnitude of these peaks is directional dependent. It is also worth to mention that the resonance spectra in these experiments all have major peaks around 1300 Hz, even though this is not always the dominate frequency among the strain signals. It is possible that such behavior is related to the nonlinear behavior of the vibrating composite plates. It also has to be mentioned that the Young's modulus of all composite plates is smaller than that of the aluminum plates, which means that the plates' vibration magnitude caused by same shock loading is larger compared with the experiments with aluminum. Again this may intensify the nonlinear effects on the plate deformation, acoustic pressure excitation and transfer.

5. Computational analysis and results

5.1. Forced axisymmetric motions of circular elastic plates

The plate is modelled by the Poisson–Kirchoff plate theory [16] and a time-dependent solution is obtained by modal superposition which has been later employed to model the dynamic response of a plate subject to shock wave loading.

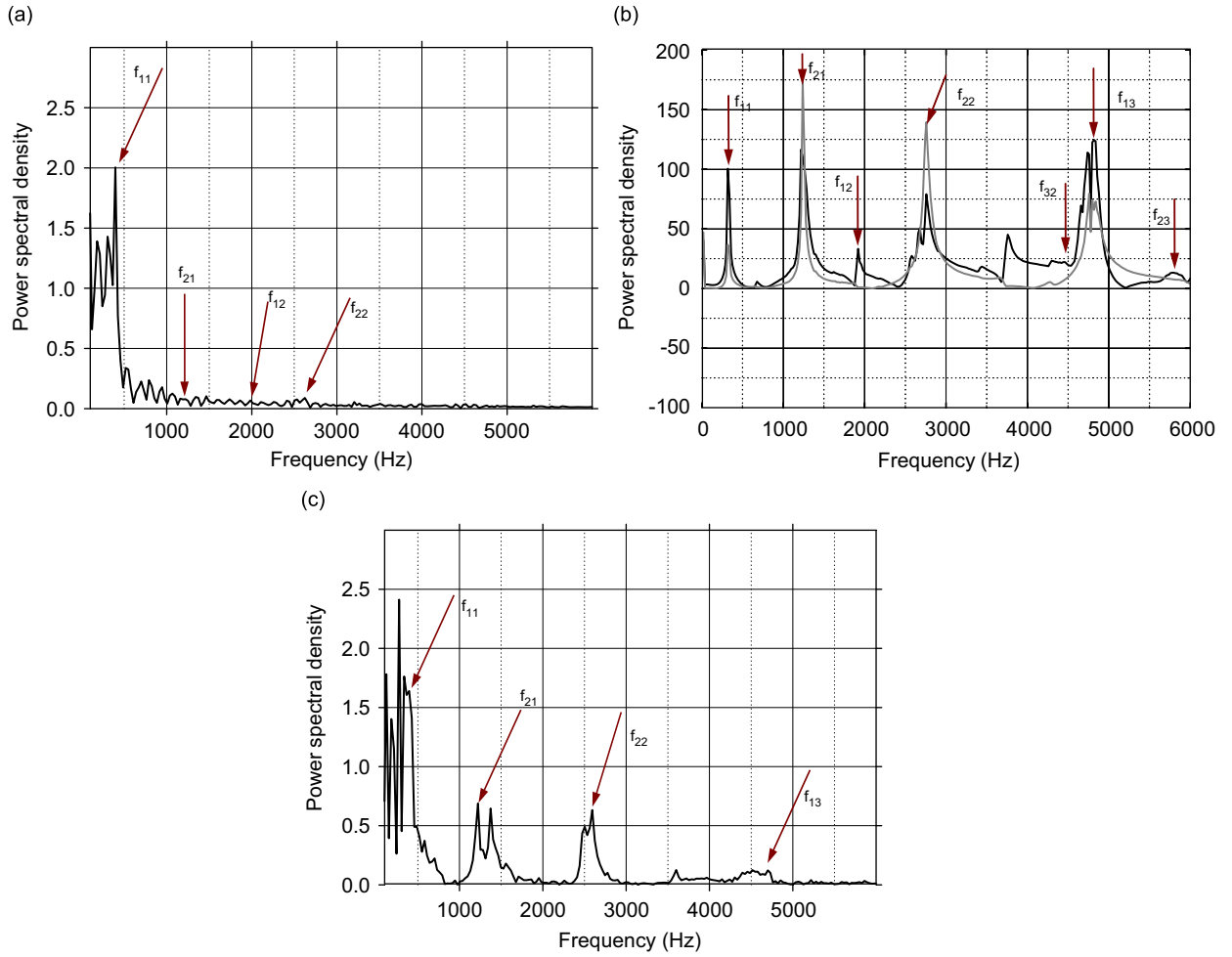

Fig. 13. (a) Power spectral density of strain gauge signal on composite plate #3. Arrows point modes according to Poisson–Kirchoff theory. (b) Power spectral density of accelerometer signals in free vibration experiments with composite plate #3. Black line, experiment #1 and gray line, experiment #2. Arrows point modes according to Poisson–Kirchoff theory. (c) Power spectral density of the pressure excited by the reverberating composite plate #3. Arrows point modes according to Poisson–Kirchoff theory.

5.1.1. *Poisson– Kirchoff formulation*

The partial differential equation of motion for the axisymmetrically loaded isotropic plate, can be expressed as

$$\nabla^4 w(r,t) + \frac{m}{D}\frac{\partial^2 w(r,t)}{\partial t^2} = \frac{p(r,t)}{D}, \tag{2}$$

where $w(r,t)$ is the transverse deflection of plate; h is the thickness of the plate; m is the mass per unit area of plate; D is the flexural rigidity of plate, $D = Eh^3/12(1-v^2)$, with E and v as the Young's modulus and Poisson's ratio, respectively; $p(r,t)$ is pressure loading on the plate.

It is assumed that in-plane forces are small compared to the forces in the normal direction of the plate because of the large amplitude of shock wave loading. As a result transverse shear stresses are ignored when the plate is undergoing small deflection.

The equation of motion has been solved with the following boundary and initial condition: (1) $w(0,t)$ must be finite; (2) $\partial w(0,t)/\partial r = 0$; (3) $w(a,t) = 0$, a is the radius of plate; (4)$-D\left[\partial^2 w(a,t)/\partial r^2 + (v/a)\left(\partial w(a,t)/\partial r\right)\right] = \beta \partial w(a,t)/\partial r$, where β is the edge spring constant of proportionality; and (5) $w(r,0) = 0$, (6) $\partial w(r,0)/\partial t = 0$.

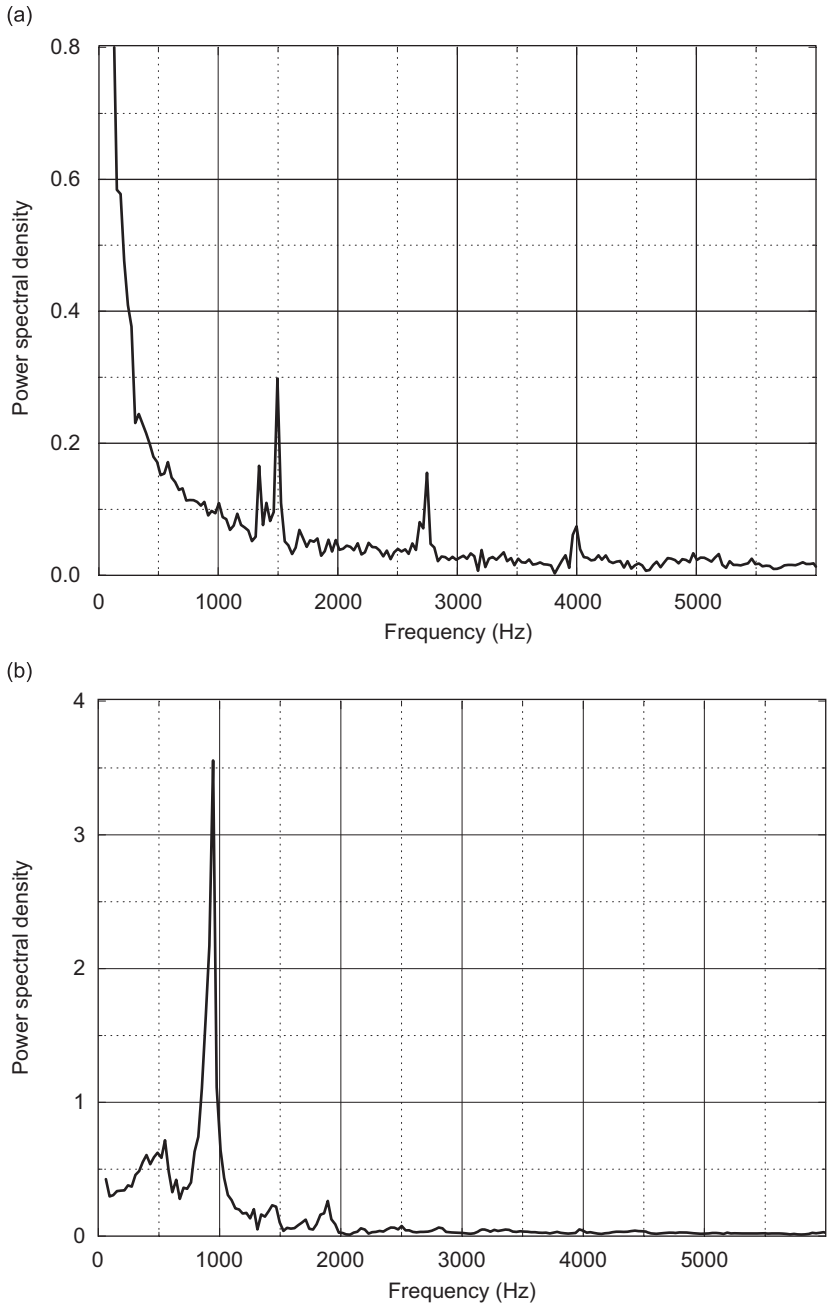

Fig. 14. (a) Power spectral density of resonance pressure in case of a composite plate with $[0]_{12}$. (b) Power spectral density of strain at location 2 in case of a composite plate with $[0]_{12}$.

These initial conditions indicate that initially the plate has no deflection and is at rest. Introducing the dimensionless quantities $\rho = r/a$ and $\eta = w/a$, Eq. (2) becomes

$$\nabla^4\eta(\rho,t) + \frac{ma^4}{D}\frac{\partial^2\eta(\rho,t)}{\partial t^2} = \frac{a^3 p(\rho,t)}{D}. \tag{3}$$

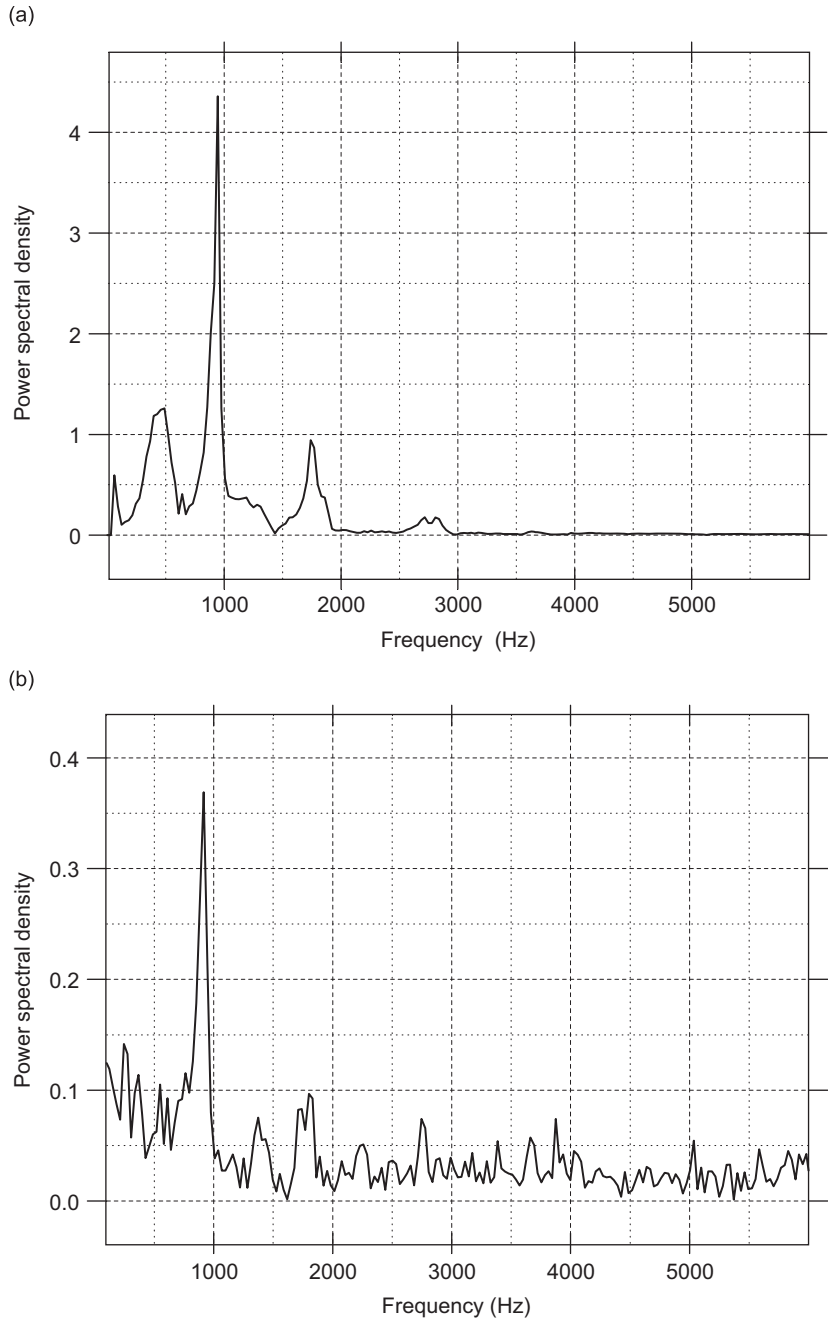

Fig. 15. (a) Power spectral density of strain at location 3 in case of a composite plate with $[0, 90]_6$. (b) Power spectral density of strain at location 3 in case of a composite plate with $[0, 45, -45, 90]_3$.

The third and fourth boundary conditions become: $\eta(1,t) = 0$ at the edge of the plate:

$$-D\left[\frac{\partial^2\eta(\rho,t)}{\partial\rho^2} + v\frac{\partial\eta(\rho,t)}{\partial\rho}\right] = a\beta\frac{\partial\eta(\rho,t)}{\partial\rho}, \tag{4}$$

at $\rho = 1$.

First, the eigenfunctions for the homogeneous equation are determined for the elastically built-in plate. Setting $p(\rho,t) = 0$ in Eq. (3) and assuming separable solutions in the form

$$\eta(\rho, t) = R(\rho)\, e^{i\Omega t}. \tag{5}$$

The ordinary differential equation resulting is

$$\left[\left(\frac{d^2}{d\rho^2} + \frac{1}{\rho}\frac{d}{d\rho}\right)^2 - \frac{ma^4}{D}\Omega^2\right] R(\rho) = 0. \tag{6}$$

The general solution of the above equation may be written as

$$R(\rho) = C_0 J_0(\kappa\rho) + C_1 Y_0(\kappa\rho) + C_2 I_0(\kappa\rho) + C_3 K_0(\kappa\rho), \tag{7}$$

where

$$\kappa^2 = a^2\left(\frac{m}{D}\right)^{1/2}\Omega.$$

J_0 is the Bessel function of the first kind; Y_0 is Bessel function of the second kind; I_0 is the modified Bessel function of the first kind; K_0 is the modified Bessel function of the second kind. C_{0-3} are constants dependent on the boundary conditions and yet to be determined. C_1 and C_3 must be zero in order to satisfy the first two boundary conditions. Boundary condition 3 is satisfied by selecting C_0 and C_2 as follows:

$$R(\rho) = I_0(\kappa)J_0(\kappa\rho) - J_0(\kappa)I_0(\kappa\rho). \tag{8}$$

When the above equation was introduced into boundary condition (4), transcendental equation for the determination of the eigenvalues, κ_i was obtained as

$$\frac{2\kappa_i}{1 - \beta a/D - \nu} = \frac{J_1(\kappa_i)}{J_0(\kappa_i)} + \frac{I_1(\kappa_i)}{I_0(\kappa_i)}. \tag{9}$$

The dimensionless ratio $\beta a/D$ will be referred to as the edge fixity parameter.

A series solution for $\eta(\rho,t)$ in equation is assumed in the form of

$$\eta(\rho, t) = \sum R_j(\rho) g_j(t), \tag{10}$$

where

$$R_j(\rho) = I_0(\kappa_j)J_0(\kappa_j\rho) - J_0(\kappa_j)I_0(\kappa_j\rho). \tag{11}$$

$g_j(t)$, which depends on the loading function, the structural plate parameters, and boundary conditions, is now to be determined.

Substituting into and interchanging the order of differentiation and summation gives

$$\sum\left\{g_j(t)\left(\frac{d^2}{d\rho^2} + \frac{1}{\rho}\frac{d}{d\rho}\right)^2 R_j(\rho) + \frac{ma^4}{D}\frac{d^2 g_j(t)}{dt^2} R_j(\rho)\right\} = \frac{a^3}{D} p(\rho, t). \tag{12}$$

Exploiting the fact that $R_j(\rho)$ satisfies the homogeneous equation, the equation above can be reduced to

$$\sum\left\{g_j(t)\kappa_j^4 + \frac{ma^4}{D}\frac{d^2 g_j(t)}{dt^2}\right\} R_j(\rho) = \frac{a^3}{D} p(\rho, t). \tag{13}$$

Multiplying both sides of the above equation by $\rho R_i(\rho)\, d\rho$ and integrating from $\rho = 0 \to 1$, by virtue of the orthogonality property, we can obtain

$$\left\{\frac{d^2 g_j(t)}{dt^2} + \frac{\kappa_j^4 D}{ma^4} g_j(t)\right\} N_{ij} = \frac{1}{ma}\int_0^1 \rho p(\rho, t) R_i(\rho)\, d\rho, \tag{14}$$

where N_{ij} is

$$N_{ij} = \left\{ \frac{1}{2}[I_0^2(\kappa_j)J_1^2(\kappa_j) - J_0^2(\kappa_j)I_1^2(\kappa_j)] - \frac{1+\nu+\beta a/D}{1-\nu-\beta a/D} I_0^2(\kappa_j)J_0^2(\kappa_j) \right\} \delta_{ij}. \tag{15}$$

In addition to the axisymmetric solution described above, non-axisymmetric solutions were calculated by considering an azimuthal variation in the modal analysis of the free vibration of circular plates according to Graff [26]. In this case, solutions in the form

$$\eta(\rho, \theta, t) = R(\rho)\Theta(\theta)\, e^{i\Omega t} \tag{16}$$

have been obtained, assuming separable solutions is possible. The complete derivation of the solution is described in Ref. [26] and when boundary condition (4) is applied, transcendental equation for the determination of the eigenvalues, $\kappa_{n,m}$ is obtained as

$$\frac{J_{n+1}(\kappa_{n,m})}{J_n(\kappa_{n,m})} + \frac{I_{n+1}(\kappa_{n,m})}{I_n(\kappa_{n,m})} = 0, \tag{17}$$

where J_n is the Bessel function of the first kind; I_n is the modified Bessel function of the first kind.

The eigenfrequencies of the plate were evaluated numerically from the above relations in a C++ program and the results for an aluminum and a stainless steel plate are tabulated in Tables 2a and b.

Attempts have also been made to simulate the response of a plate subject to a shock wave impact loading by using Eq. (15). The raw pressure history obtained by experiment is shown in Fig. 16.

In the experiment this pressure signal was measured with a pressure transducer mounted on the center of the plate and the corresponding raw strain signal from one strain gage near center at $r = 0.5''$ is shown in Fig. 17. The numerical results obtained by using Eq. (15) are also presented in Fig. 17 for a direct comparison. It can be seen that the numerically calculated strain is significantly different from the experimental one. There may be several reasons for this disagreement: (1) Eq. (15) is the solution of (2), which neglects the damping effect. However, experimental data show that damping plays a substantially important role in this problem. Thus a new mathematical model which considers the damping effect is required for an appropriate approach to this problem. (2) The signal in Fig. 17 shows that the displacement is mostly consisted by the first mode of the plate. The numerical evaluation also shows that the second mode of the vibration is of a magnitude of 1/100th

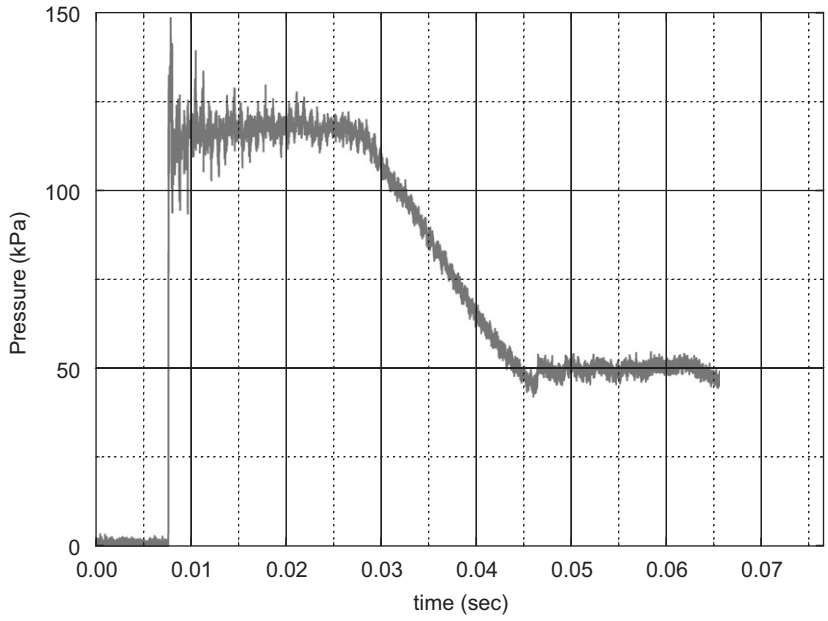

Fig. 16. Pressure signal used for numerical evaluation.

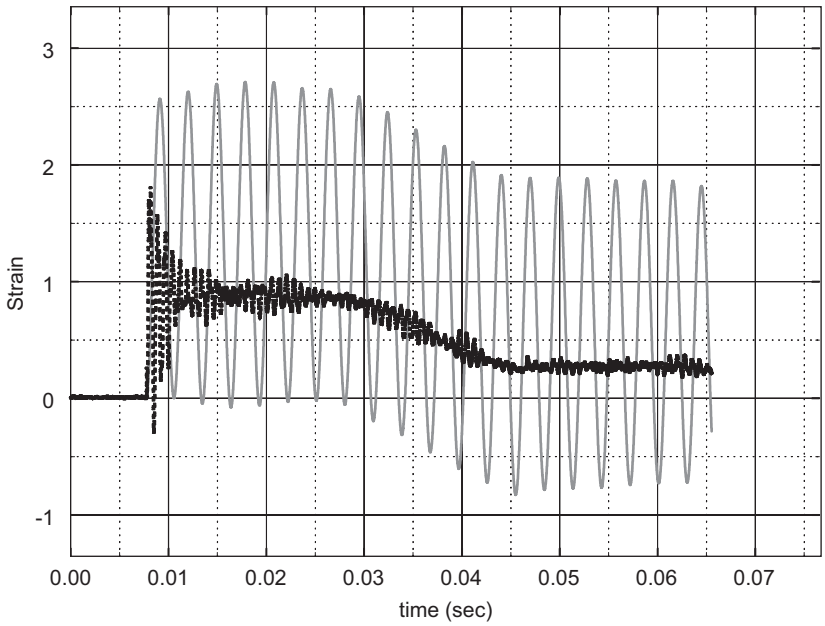

Fig. 17. Experimental strain–time history multiplied by 10^4 (--------). Strain–time history obtained from Eq. (15) multiplied by 10^3 (gray line).

of the first mode. However, experiments show that the first mode is somehow suppressed and its amplitude is of the same order as the second mode.

5.2. Coupled fluid–structure vibration modal analysis with finite element method

The problem of free vibrating plate coupled with fluid can be analyzed using finite element method, where the structure and fluid matrix equations were merged together and then solved [27,28].

In finite element form, the discrete structural problem of a vibrating plate can be described by

$$[\mathbf{K}]\{\mathbf{u}_i\} + [\mathbf{C}]\frac{\partial\{\mathbf{u}_i\}}{\partial t} + [\mathbf{M}]\frac{\partial^2\{\mathbf{u}_i\}}{\partial t^2} - \frac{1}{\rho_F}[\mathbf{Q}]\{\mathbf{p}_i\} + \{\mathbf{R}\} = 0, \tag{18}$$

where $[\mathbf{K}]$ is the stiffness matrix; $[\mathbf{C}]$ is the matrix of viscous damping terms; $[\mathbf{M}]$ is the mass matrix; $\{\mathbf{R}\}$ is the external forcing function; $[\mathbf{u}_i]$ is the structure displacement vector; ρ_F is the density of the fluid; $\{\mathbf{p}_i\}$ is the fluid's pressure vector; $-(1/\rho_F)[\mathbf{Q}]\{\mathbf{p}_i\}$ is the fluid structure coupling term, which is caused by the pressure specified on the fluid–structure boundary and

$$\begin{gathered}[\mathbf{Q}] = \sum[q],\\ [q] = \int_S \rho_F[\mathbf{S}]^{\mathrm{T}}(-\mathbf{n}_s)[\mathbf{N}]\,\mathrm{d}S = \int_S \rho_F[\mathbf{S}]^{\mathrm{T}}\mathbf{n}[\mathbf{N}]\,\mathrm{d}S,\end{gathered} \tag{19}$$

where $[\mathbf{N}]$ is the shape functions for the fluid element; $[\mathbf{S}]$ is the shape function of the structure; $\mathrm{d}S$ is the elemental area at fluid–plate interface; p is pressure and defined positive as compression. On the fluid–structure interface, we have

$$-p\mathbf{n}_s = p\mathbf{n},$$

where $\mathbf{n}_s$ and $\mathbf{n}$ are surface outward normals to the solid and fluid, respectively.

For free vibrations without damping, Eq. (18) reduces to

$$[\mathbf{K}]\{\mathbf{u}_i\} + [\mathbf{M}]\frac{\partial^2\{\mathbf{u}_i\}}{\partial t^2} - \frac{1}{\rho_F}[\mathbf{Q}]\{\mathbf{p}_i\} = 0. \tag{20}$$

The following wave equation for the non-viscous, compressible fluid is used to represent the motion of the fluid:

$$\nabla^2 p - \frac{1}{c^2}\frac{\partial^2 p}{\partial t^2} = 0, \tag{21}$$

where p is the pressure in the fluid, and c is the sound speed of the fluid, i.e., the propagation speed of small disturbance waves in the fluid. Using the calculus of variations, the above wave equation can be expressed in discrete finite element form as

$$[\mathbf{H}]\{\mathbf{p}_i\} - [\mathbf{G}]\frac{\partial^2\{\mathbf{p}_i\}}{\partial t^2} + [\mathbf{Q}]^{\mathrm{T}}\frac{\partial^2\{\mathbf{u}_i\}}{\partial t^2} = 0, \tag{22}$$

where $\{\mathbf{p}_i\}$ is vector of fluid nodal pressure caused by structure vibration; $\{\mathbf{u}_i\}$ is vector of structure nodal displacement; $[\mathbf{H}]$ is in a form similar to the stiffness matrix of the structure, it may be considered as the fluid's virtual stiffness matrix

$$\begin{aligned}[\mathbf{H}] &= \sum[h],\\ [h] &= \int_{\mathrm{vol}}\left\{\frac{\partial[\mathbf{N}]^{\mathrm{T}}}{\partial x}\frac{\partial[\mathbf{N}]}{\partial x} + \frac{\partial[\mathbf{N}]^{\mathrm{T}}}{\partial y}\frac{\partial[\mathbf{N}]}{\partial y} + \frac{\partial[\mathbf{N}]^{\mathrm{T}}}{\partial z}\frac{\partial[\mathbf{N}]}{\partial z}\right\}\mathrm{d}V,\end{aligned} \tag{23}$$

where $[\mathbf{N}]$ is the shape functions for the fluid element; $[\mathbf{G}]$ is in a form similar to the mass matrix of the structure, it may be considered as the fluid's virtual mass matrix

$$\begin{aligned}[\mathbf{G}] &= \sum[g],\\ [g] &= \frac{1}{c^2}\int_{\mathrm{vol}}[\mathbf{N}]^{\mathrm{T}}[\mathbf{N}]\,\mathrm{d}V,\end{aligned} \tag{24}$$

where c is the speed of sound as described before; $[\mathbf{Q}]^{\mathrm{T}}\partial^2\{\mathbf{u}_i\}/\partial t^2$ is the fluid structure coupling term, which is the pressure force acting in the surface normal direction on the fluid–structure interface,

$$\begin{aligned}[\mathbf{Q}] &= \sum[q],\\ [q] &= \int_S \rho_F[\mathbf{S}]^{\mathrm{T}}\mathbf{n}[\mathbf{N}]\,\mathrm{d}S,\end{aligned} \tag{25}$$

where ρ_F is the density of the fluid; $[\mathbf{S}]$ is the shape function of the structure element; $\mathbf{n}$ is the fluid outward surface normal; note that when deriving this coupling force term, the relationship

$$\frac{\partial p}{\partial n} = -\rho_F\dot{v}_n = -\rho_F\mathbf{n}^{\mathrm{T}}\cdot\frac{\partial^2\mathbf{u}}{\partial t^2} \tag{26}$$

is used, where v_n is the fluid velocity at the fluid–structure interface boundary, caused by the motion of the structure, which is then described by $\mathbf{n}^{\mathrm{T}}\dot{\mathbf{u}}$. The underlying assumptions in this relationship are that the fluid is under very small disturbance such that the convection term can be neglected; and the density of the fluid ρ_F varies by a small amount only so that it may be considered constant. In the integral above, $\mathrm{d}S$ is the elemental area at fluid–plate interface and $\mathrm{d}V$ is the elemental volume.

If the fluid–structure vibrates with simple harmonic motion, we can assume that the vector of nodal acoustic pressure $\{\mathbf{p}_i\}$ and the vector of nodal displacements $\{\mathbf{u}_i\}$ is given by: $\{\mathbf{p}_i\} = \{\mathbf{p}_0\}\cos\omega t$ and $\{\mathbf{u}_i\} = \{\mathbf{u}_0\}\cos\omega t$.

Coupling Eqs. (19) and (20) leads to the following sets of simultaneous equations:

$$\begin{bmatrix}[\mathbf{K}] & -[\mathbf{Q}]^{\mathrm{T}}/\rho_F\\ [\mathbf{0}] & [\mathbf{H}]\end{bmatrix}\begin{bmatrix}\mathbf{u}_0\\ \mathbf{p}_0\end{bmatrix} - \omega^2\begin{bmatrix}[\mathbf{M}] & [\mathbf{0}]\\ [\mathbf{Q}] & [\mathbf{G}]\end{bmatrix}\begin{bmatrix}\mathbf{u}_0\\ \mathbf{p}_0\end{bmatrix} = \mathbf{0}, \tag{27}$$

where ω is radian frequency. The solution of Eq. (25) is not convenient because it is unsymmetrical. However, we can rearrange Eq. (25) using the bottom row of the equation:

$$\{\mathbf{p}_0\} = [\mathbf{H}]^{-1}\omega^2([\mathbf{G}]\{\mathbf{p}_0\} + [\mathbf{Q}]\{\mathbf{u}_0\}). \tag{28}$$

The symmetrical form of Eq. (27) is

$$\left\{ \begin{bmatrix} \rho_F[\mathbf{K}] & [\mathbf{0}] \\ [\mathbf{0}] & [\mathbf{H}] \end{bmatrix} - \omega^2 \begin{bmatrix} \rho_F[\mathbf{M}] + [\mathbf{Q}]^{\mathrm{T}}[\mathbf{H}]^{-1}[\mathbf{Q}] & [\mathbf{Q}]^{\mathrm{T}}[\mathbf{H}]^{-1}[\mathbf{G}] \\ [\mathbf{G}][\mathbf{H}]^{-1}[\mathbf{Q}] & [\mathbf{G}][\mathbf{H}]^{-1}[\mathbf{G}] \end{bmatrix} \right\} \begin{bmatrix} \mathbf{u}_0 \\ \mathbf{p}_0 \end{bmatrix} = \mathbf{0}. \tag{29}$$

Considering the case for incompressible fluid, $[\mathbf{G}] = 0$, Eq. (29) becomes

$$\rho_F[\mathbf{K}] - \omega^2(\rho_F[\mathbf{M}] + [\mathbf{Q}]^{\mathrm{T}}[\mathbf{H}]^{-1}[\mathbf{Q}]) = 0, \tag{30}$$

where

$$\frac{1}{\rho_F}[\mathbf{Q}]^{\mathrm{T}}[\mathbf{H}]^{-1}[\mathbf{Q}] \tag{31}$$

is the added virtual mass.

A C++ program is employed to implement the above theory to solve for the natural frequency of a plate vibrating in air. Fig. 18 shows a circular plate divided into 16 elements with five fluid layers. The material properties used in the calculation is listed in previous chapter (Table 1a). The properties of fluid (air) used for this computation are $\rho_F = 1.293\,\mathrm{kg/m^3}$ for fluid density and 0.53 m for fluid layer thickness.

It is always useful to compare the predicted values of the eigenfrequencies of the metallic and isotropic composite plates shown in Table 2a–c by using the three methods described above with those measured in the free and forced vibration experiments. In the case of aluminum plates, the agreement between the predicted values of the first mode and the measured data improves with increasing model complexity. It is shown in this case that the coupled finite element analysis provided predictions closer to measured values than the classical modal analysis. The coupled fluid–structure calculation yields a lower eigenfrequency compared with that of non-coupled calculation, which is obvious as a result of the added virtual mass term in the coupled solution. In the case of higher modes, however, the first two methods provide reasonable agreement with experimental data.

In the cases of monolithic materials, the predicted values of eigenfrequencies appear to be in reasonable agreement with the experimental ones. However, this agreement is less satisfactory in the case of isotropic composite plates, a behavior most probably due to limitations in the theory which takes into account equivalent monolithic material properties from the two composing materials of the composite plates. In addition, several of the assumptions made in the theory, not only for composites but for monolithic materials

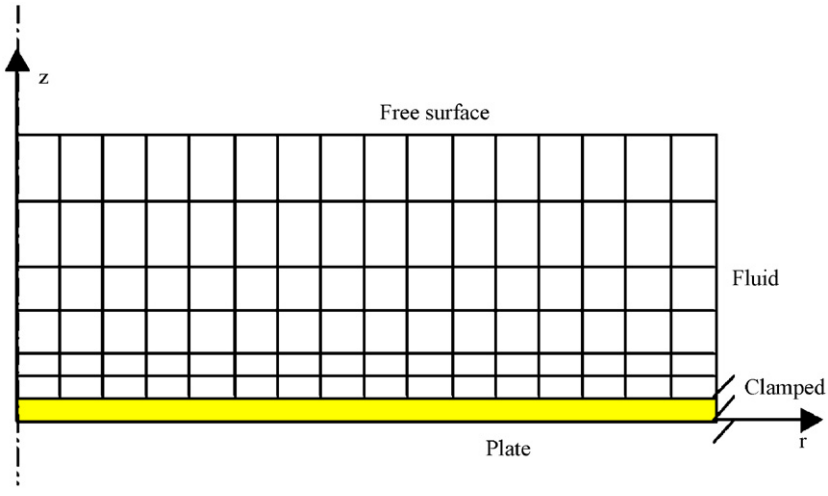

Fig. 18. Coupled fluid–structure numerical simulation of a vibrating plate.

too, are not met in the experiments. For instance, the assumption of rigidity adopted in the theory is not entirely valid because some plasticity has been observed in the shock loaded experiments.

6. Conclusions and final remarks

The present investigation was aimed at better understanding of the shock wave impact on metallic and composite plates. Experiments were carried out in a shock tube facility to investigate the aero-elastic response of fully clamped thin circular plates during face-on impact with planar shock waves. High-frequency response dynamic strain history was obtained on various locations of the plate and measurement of acoustic pressure excited by the vibrating plate was performed as well. Experimental results show that plates made of different material exhibits distinct modal response when subject to shock wave loading.

Additional free vibration tests by using an accelerometer provided the modal content of the motion of the plates.

Analytical formulas based on Poisson–Kirchoff theory were employed to determine the modal frequency. Finite element analysis revealed that modal frequency calculated by using a coupled system of equations between the fluid and solid phases of monolithic materials provided predictions closer to measured values of the first mode only than that with classical modal analysis.

Spectral analysis of the signals indicated that most of the energy in metallic plates is distributed over a wide range of frequencies. The experiments with composite plates indicated that the shock impact results in one basic mode of strain only and most probably dampens all others by mechanisms that do not play any role or do not exist in relatively monolithic materials. The difference in the propagation and transmission of compressive or shearing waves inside the reinforcing fibers and inside the matrix and their mutual interaction during the sudden loading of the composite plates results in a complex dynamic performance which appears to be very preferential. The process of simple flexure entails a dashpot effect due to the nearly viscoelastic behavior of matrices. The relatively compliant yet resistive movement of the material absorbs fluid energy, which is then dissipated into heat by relaxation processes of viscoelasticity. Although the strain field indicates considerable damping of several of the modes, reverberation of the plate at one or more modes can excite additional modes in the acoustic field as the pressure spectra in Fig. 15 have indicated. Further investigation is needed in order to better understand these phenomena. This interesting behavior of shock wave-composite plate interaction may have an adverse effect on the survivability of a composite enclosure and the personnel and equipment contained inside if material selection and structural design are not carried out carefully.

There is a remarkable similarity in the modal content of the motion of all plates in free vibration. Even in the case of composites where the strain field shows limited number of excited modes in forced vibrations, a large number of modes is excited. This suggests that, physically, the motion of all plates, as this is depicted by their surface acceleration, is the same regardless of the constituting material. However, this is not true in the internal wave stress field where local discontinuities in composite material properties increase complexity in modal interaction which may suppress many modes.

Numerical simulations and analytical results for the case of monolithic materials provided reasonable good predictions of the first vibrating modes, particularly those involving the coupled equations between the fluid and solid phases. Due to the complexity of the phenomena involved, no attempt has been made to compute the structural response of composite material plates by using the same equations with equivalent composite material properties which cannot reproduce their preferential behavior of damping higher modes.

The mechanisms involved in the shock wave impact on a flat plate and the subsequent transient aero-elastic interaction between them are quite complicated. The ''face-on'' shock reflection over a rigid flat surface occurs suddenly at the moment when the shock starts in contact with the surface. Thus shock reflection starts at the same time at all locations of contact. If the mass of the plate and therefore its characteristic time is of the same order as that of the shock wave the plate can start deforming before the shock wave reflection is completed. In the present case, the shock wave has a time scale that is much faster than the time scale of the plates and therefore its reflection is over before the deformation of the plate.

It was also observed that there exists a nonlinear acoustic excitation by the plate. Damping of the plate vibration in time was also observed on all plates during the interaction.

Acknowledgments

The authors would like to acknowledge the financial support provided by the US Army Research Development and Engineering Center (ARDEC) at Picatinny Arsenal. Useful discussions with Ben Liaw, Kolluru Subramaniam and Feridun Delale are appreciated.

References

[1] B. Hopkinson, British Ordnance Board Minutes, Report No. 13565, British Ordnance Office, London, 1915.
[2] G.I. Taylor, *The Pressure and Impulse of Submarine Explosion Waves on Plates, Vol. III of The Scientific Papers of G.I. Taylor*, Cambridge University Press, Cambridge, UK, 1963.
[3] R. Houlston, J.E. Slate, N. Pegg, C.G. DesRochers, On analysis of structural response of ship panels subjected to air blast loading, *Computers and Structures* 26 (1987) 1–15.
[4] A.D. Gupta, F.H. Gregory, R.L. Bitting, S. Bhattacharya, Dynamic analysis of an explosively loaded hinged rectangular plate, *Computers and Structures* 26 (1987) 339–344.
[5] F.B.A. Beshara, Modeling of blast loading on aboveground structures—I. General phenomenology and external blast, *Computers and Structures* 51 (1994) 585–596.
[6] H.S. Turkmen, Z. Mecitoglu, Nonlinear structural response of laminated composite plates subjected to blast loading, *AIAA Journal* 37 (12) (1999) 1639–1647.
[7] H.S. Turkmen, Z. Mecitoglu, Dynamic response of stiffened laminated composite plate subjected to blast load, *Journal of Sound and Vibration* 221 (1999) 371–389.
[8] A.C. Jacinto, R.D. Ambrosini, R.F. Danesi, Experimental and computational analysis of plates under air blast loading, *International Journal of Impact Engineering* 25 (2001) 927–947.
[9] S. Chung Kim Yuen, G.N. Nurick, Experimental and numerical studies on the response of quadrangular stiffened plates, part I: subjected to uniform blast load, *International Journal of Impact Engineering* 31 (2005) 55–83.
[10] Z. Xue, J.W. Hutchinson, Preliminary assessment of sandwich plates subject to blast loads, *International Journal of Mechanical Sciences* 45 (2003) 687–705.
[11] Z. Xue, J.W. Hutchinson, A comparative study of impulse-resistant metal sandwich plates, *International Journal of Impact Engineering* 30 (2004) 1283–1305.
[12] N.A. Fleck, V.S. Deshpande, The resistance of clamped sandwich beams to shock loading, *Journal of Applied Mechanics, Transactions of the ASME* 71 (2004) 386–401.
[13] X. Qiu, V. Deshpande, N. Fleck, Dynamic response of a clamped circular sandwich plate subject to shock loading, *Journal of Applied Mechanics, Transactions of the ASME* 71 (2004) 637–645.
[14] G.C. Mays, P.D. Smith, *Blast Effects on Buildings*, Thomas Telford, London, 1995.
[15] A.M. Saad, *Compressible Flow*, Prentice-Hall, Englewood Cliffs, NJ, 1984.
[16] R.S. Weiner, Forced axisymmetric motions of circular elastic plates, *Journal of Applied Mechanics* (1965) (paper no. 65-APMW-7).
[17] G. Briassulis, J.H. Agui, J. Andreopoulos, B.C. Watkins, A shock tube research facility for high-resolution measurements of compressible turbulence, *Experimental Thermal and Fluid Science* 13 (1996) 430–446.
[18] Y. Andreopoulos, J.H. Agui, G. Briassulis, Shock wave turbulence interactions, *Annual Review of Fluid Mechanics* 32 (2000) 309–345.
[19] J.H. Agui, G. Briassulis, Y. Andreopoulos, Studies of interactions of a propagating shock wave with decaying grid turbulence: velocity and vorticity field, *Journal of Fluid Mechanics* 524 (2005) 143–195.
[20] G. Briassulis, J.H. Agui, Y. Andreopoulos, The structure of weakly compressible grid turbulence, *Journal of Fluid Mechanics* 432 (2001) 219–283.
[21] C.H. Lamarque, S. Pernot, A. Cuer, Damping identification in multi-degree-of-freedom systems via a wavelet logarithmic decrement—part 1: theory, *Journal of Sound and Vibration* 235 (2000) 361–374.
[22] M. Gong, Mutual Interactions between Shock Waves and Structures, PhD Thesis, City University of New York, 2006.
[23] Y. Andreopoulos, M. Gong, Z. Wang, S. Xanthos, A probe to measure direction and strength of moving shocks or blast waves, *American Institute of Aeronautics and Astronautics Journal* 41 (2003) 476–484.
[24] S. Xanthos, G. Briassulis, Y. Andreopoulos, The interaction of decaying free stream turbulence with a moving shock wave: pressure field, *American Institute of Aeronautics and Astronautics Journal of Propulsion and Power* 18 (2002) 1289–1297.
[25] A. Frendi, L. Maestrello, A. Bayliss, Coupling between plate vibration and acoustic radiation, *Journal of Sound and Vibration* 177 (1994) 207–226.
[26] K.F. Graff, *Wave Motion in Elastic Solids*, Dover, New York, 1991.
[27] C.T.F. Ross, *Finite Element Programs for Axisymmetric Problems in Engineering*, Wiley, New York, 1984.
[28] O.C. Zienkiewicz, R.L. Taylor, *The Finite Element Method*, Butterworth-Heinemann, London, 2000.